Chemical Science

ROYAL SOCIETY OF CHEMISTRY

EDGE ARTICLE

View Article Online
View Journal | View Issue

Cite this: *Chem. Sci.*, 2025, **16**, 12927

All publication charges for this article have been paid for by the Royal Society of Chemistry

Dual-engine-driven synthesis of unsaturated esters over channel-expanding Cu–Cs catalysts†

Jiaqi Fan,[ab] Lishu Shao,*[bc] Weizhe Gao,[b] Yitong Han,[b] Wenjie Xiang,[b] Hao Huang,[b] Zhihao Liu,[b] Chufeng Liu,[b] Bo Wang,[b] Kangzhou Wang,[d] Guangbo Liu,[e] Jiancai Sui,[f] Qiang Liu,[f] Tao Li,[g] Tao Xing,[g] Shuhei Yasuda,[b] Zhixin Yu,*[a] Guohui Yang,*[bh] Peipei Zhang*[i] and Noritatsu Tsubaki*[b]

Received 21st April 2025
Accepted 10th June 2025

DOI: 10.1039/d5sc02896e

rsc.li/chemical-science

This study presents a one-step catalytic synthesis of unsaturated esters (methyl acrylate, MA; methyl methacrylate, MMA) from methanol (MeOH, C1 source) and methyl acetate (MAc) *via* a Cu–Cs dual-engine-driven (DED) system that integrates four sequential steps—dehydrogenation, aldol condensation, hydrogenation, and secondary aldol condensation. The Cu-engine facilitates proton transfer by capturing protons during MeOH dehydrogenation and donating them in methyl acrylate (MA) hydrogenation, while the Cs-engine activates saturated esters for formaldehyde-mediated aldol condensation. Through systematic optimization of Cu loading methods, deposition sequences, and Cu/Cs ratios, we developed a silicon carrier channel-expanding strategy, enlarging mesopores from 14 nm to 20 nm (30% specific surface area extension) *via* copper phyllosilicate-induced corrosion. Catalytic performance hinges on balanced medium-strength acid–base sites, a 10 : 7 Cs/Cu ratio, and sequential Cu/Cs loading *via* the ammonia evaporation method. The optimized 10Cs/7Cu/Q10 catalyst, combined with a downstream Cs–Al/Q10 system, achieves 64.0% unsaturated ester selectivity (55.3% MeOH and 59.8% methyl acetate conversion). This work establishes a design framework for efficient Cu–Cs catalysts in one-step ester synthesis, emphasizing pore engineering, acid–base synergy, and dual-site cooperativity.

Introduction

Short-chain unsaturated esters, methyl acrylate (MA) and methyl methacrylate (MMA), serve as pivotal chemical feedstocks with extensive applications spanning adhesives, coatings, functional materials and the modification of plastics and rubber.[1–8] Notably, polymethyl methacrylate (PMMA), synthesized from MMA monomers, assumes an irreplaceable role in biomedical applications,[9–11] underscoring the paramount importance of efficient MMA production methodologies.

Currently, industrial synthesis of MMA predominantly relies on acetone-, isobutene- or ethylene-based routes.[12] The acetone cyanohydrin (ACH) process, utilizing acetone as the starting material, necessitates the use of highly toxic hydrogen cyanide (HCN) and excessive corrosive sulfuric acid during the amination step,[13] posing significant safety and environmental challenges. Isobutylene-derived processes *via* methacrolein intermediates are encumbered by the reliance on rare metal catalysts and complex multi-step procedures.[14–17] Ethylene-based pathways include hydroesterification and aldol condensation;[18–20] the former step demands palladium-based catalysts, inflating industrial costs, while the latter step, involving methyl propionate (MP)-formaldehyde condensation under milder conditions, emerges as a promising alternative. Besides ethylene, MP can also be produced by the hydrogenation of MA. Therefore, a three-step cascade process involving aldol condensation, hydrogenation and secondary aldol condensation using formaldehyde and methyl acetate (Mac) as feedstocks offers an environmentally benign route to MMA (Fig. 1). However, this approach requires either dissolving toxic paraformaldehyde in methanol (MeOH) or oxidizing MeOH to

[a]*Institute of New Energy, School of Chemistry and Chemical Engineering, Shaoxing University, Shaoxing 312000, China. E-mail: zhixin.yu@uis.no*

[b]*Department of Applied Chemistry, School of Engineering, University of Toyama, Gofuku 3190, Toyama 930-8555, Japan. E-mail: tsubaki@eng.u-toyama.ac.jp; thomas@eng.u-toyama.ac.jp*

[c]*Ministry of Forestry Bioethanol Research Center, School of Materials Science and Engineering, Central South University of Forestry and Technology, Changsha, 410004, China. E-mail: lishushao@csuft.edu.cn*

[d]*School of Materials and New Energy, Ningxia University, Yinchuan, Ningxia 750021, China*

[e]*Key laboratory of Biofuels, Qingdao Institute of Bioenergy and Bioprocess Technology, Chinese Academy of Sciences, Qingdao 266101, China*

[f]*Shandong Energy Group Co., Ltd, Jinan, Shandong 250101, China*

[g]*Shandong Energy Group Coal Gasification New Materials Technology Co., Ltd., Jinan, Shandong 250220, China*

[h]*State Key Laboratory of Fine Chemicals, School of Chemical Engineering, Dalian University of Technology, Dalian, 116024, China*

[i]*CNOOC Institute of Chemical & Advanced Materials, Beijing 102209, China. E-mail: zhangpp15@cnooc.com.cn*

† Electronic supplementary information (ESI) available. See DOI: https://doi.org/10.1039/d5sc02896e

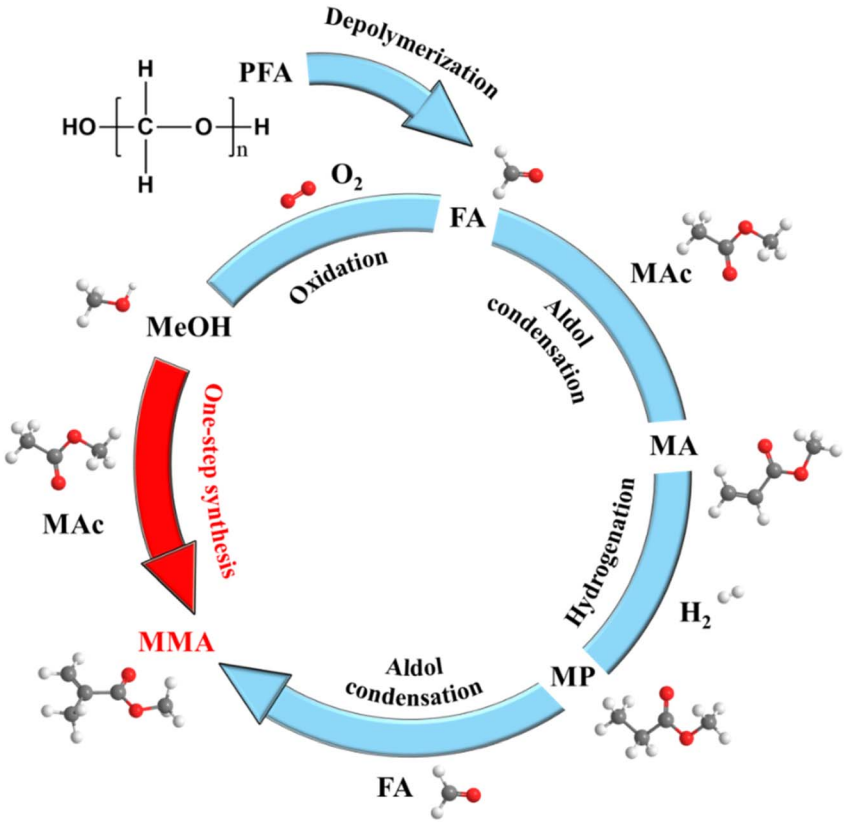

Fig. 1 Traditional process and the one-step synthesis route for MMA.

generate formaldehyde. Both methods are operationally cumbersome and economically inefficient. Direct utilization of MeOH as a feedstock for unsaturated esters could streamline the synthesis and enhance the value of this abundant C1 compound.

MeOH was primarily produced *via* syngas conversion over Cu-based catalysts[21–23] and increasingly *via* CO_2 reduction pathways.[24,25] In 2013, Tsubaki's team reported a remarkable 56% total carbon conversion and 98% MeOH selectivity at 170 °C from CO_2-containing syngas.[21] Mature synthesis routes and well-established synthesis processes render MeOH a readily available C1 resource.[26–28] Leveraging MeOH to produce high value-added products not only addresses excess production capacity but also aligns with global efforts toward carbon neutrality.

In the pursuit of more sustainable synthesis methods, numerous strategies have been explored for the catalytic conversion of MeOH into unsaturated esters. Cobalt complexes have demonstrated catalytic activity, yet their intricate molecular structures and elaborate preparation protocols impede practical implementation.[29,30] Noble metal-based systems, such as Au catalysts, exhibit excellent performance but remain cost-prohibitive for large-scale industrial deployment.[31,32] Zeolite-based catalysts, exemplified by Beta zeolites, suffer from inevitable coke formation, leading to rapid deactivation and shortened catalyst lifetimes.[33] Although Duan's team recently reported a Cu/SiO_2 and Cs/SiO_2 catalyst mixture for MMA synthesis,[34] the practical application of this system requires the precise arrangement of three distinct catalysts within the reaction bed, with product selectivity highly sensitive to their spatial configuration.

Considering the above challenges and opportunities, the design of a novel catalytic system for the one-step synthesis of MMA or MA from MeOH presents a compelling research direction. Drawing inspiration from the "dual-engine-driven" (DED) catalytic concept,[35] we hypothesized that the protons released during methanol-to-formaldehyde conversion could be harnessed for MA hydrogenation. Capitalizing on this synergy, we developed a copper–cesium-based DED catalytic system. The Cu-engine functions as a proton shuttle, facilitating proton abstraction during MeOH dehydrogenation and donation during MA reduction, while the Cs-engine activates MAc and MP, promoting their condensation with formaldehyde. This integrated approach aims to achieve a more efficient and sustainable route to industrially important unsaturated esters.

Experimental

Catalyst preparation

Supported Cu–Cs catalysts were prepared by the impregnation or ammonia evaporation method.

During a typical co-impregnation process, 0.312 g of cesium nitrate ($CsNO_3$, Sigma-Aldrich, 99%) and 0.534 g of copper nitrate ($Cu(NO_3)_2 \cdot 3H_2O$, Sigma-Aldrich, 99%) were dissolved in

5 mL of deionized water separately and stirred for 30 min. The above solutions were then added dropwise to 2 g of SiO_2 (CARiACT Q-10, Fuji Silysia Chemical Ltd.) particles under ultrasonic treatment. After vacuum drying overnight, the sample was further calcined at 500 °C for 6 h. Two samples with different metal loadings were prepared and named 10Cs–7Cu/Q10 and 33Cs–22Cu/Q10, respectively. 10Cs/Q10 was prepared by the same impregnation method without adding Cu sources.

7Cu/Q10 and 22Cu/Q10 were prepared by the ammonia evaporation method. Specifically, 0.534 g of copper nitrate ($Cu(NO_3)_2 \cdot 3H_2O$, Sigma-Aldrich, 99%) was dissolved in 50 mL of deionized water. Subsequently, 5 ml of ammonia ($NH_3 \cdot H_2O$, Wako, 25%) was added and stirred for 30 minutes, followed by the addition of 2 g of SiO_2 (CARiACT Q-10, Fuji Silysia Chemical Ltd.). The mixture was stirred at room temperature for 4 h to form a homogeneous slurry and then stirred at 80 °C for 2 h to evaporate the ammonium solution. The obtained precursors with different metal loadings were washed, dried, and then calcined at 400 °C for 4 h to obtain 7Cu/Q10 and 22Cu/Q10.

7Cu/10Cs/Q10-A was obtained by loading Cu on previously mentioned 10Cs/Q10 through ammonia evaporation treatment. 7Cu/10Cs/Q10-I was also prepared in two steps; however, Cu was loaded by the impregnation method rather than ammonia vaporization.

10Cs/7Cu/Q10 and 33Cs/22Cu/Q10 were prepared based on 7Cu/Q10 and 22Cu/Q10, with Cs loaded by the impregnation method. Meanwhile, 13Cs/4Cu/Q10 and 7Cs/10Cu/Q10 with different copper–cesium ratios were also prepared.

10Cs–Al/Q10 was prepared by two step impregnation. 0.91 g of aluminum nitrate ($Al(NO_3)_3 \cdot 9H_2O$, Wako, 98%) was dissolved in 5.1 mL of deionized water, then dropwise added to 4 g of SiO_2 (CARiACT Q-10, Fuji Silysia Chemical Ltd) and sonicated for 30 min. Al/Q10 was obtained after overnight drying and calcination at 500 °C for 4 h. Cesium carbonate (Cs_2CO_3, Sigma-Aldrich, 99%) was then dissolved in 3.3 mL of deionized water and dropped onto Al/Q10, followed by overnight drying, and further calcined by a stepwise temperature program of 150 °C for 3 h, then 350 °C for 3 h, and lastly 550 °C for 4 h to get 10Cs–Al/Q10.

7Cu/10Cs–Al/Q10 was prepared by the same method of 7Cu/10Cs/Q10-I except for the replacement of 10Cs/Q10 with 10Cs–Al/Q10.

Catalyst characterization

Powder X-ray diffraction (XRD) was performed on a RINT 2400 diffractometer (Rigaku, Japan) with a Cu Kα (λ = 0.154 nm) radiation source. The operating voltage was 40 KV, and the current was 20 mA. Scanning was carried out in the 2θ range of 5–80° W. The scanning electron microscopy (SEM) images were captured using a JSM-6360 LV (JEOL, Japan) at an accelerating voltage of 10 kV. High-resolution transmission electron microscopy (HRTEM) was performed using a JEM-2100F microscope operated at 200 kV, and elemental mapping was performed using an Oxford spectrometer.

Inductively coupled plasma-optical emission spectrometry (ICP-OES) was conducted using a Thermo Scientific iCAP at an RF power of 1.25 W. A certain amount of the sample was dissolved in mixed acids and diluted to a constant volume, followed by nebulization at a flow rate of 0.7 L min^{-1} into the spectrophotometric system.

X-ray photoelectron spectroscopy (XPS) of the samples was carried out on a Thermo Fisher Scientific ESCALAB 250Xi multifunctional X-ray photoelectron spectroscope. All data were normalized and corrected with a standard of 284.8 eV for C 1s.

The acidic and alkali properties of the samples were measured using ammonia temperature-programmed desorption (NH_3-TPD) and carbon dioxide temperature-programmed desorption (CO_2-TPD). These measurements were carried out on a BELCAT II catalyst analyzer equipped with a thermal conductivity detector (TCD). In a typical NH_3-TPD measurement, 10 mg of sample powder was pretreated for 1 h at 400 °C under a flow of helium at 30 ml min^{-1}. Then, the mixed ammonia gas flow (5 vol% NH_3/He, 30 mL min^{-1}) was introduced after cooling down to 50 °C. Subsequently, helium (30 ml min^{-1}) was purged for 1 h to remove physically adsorbed ammonia. The desorption of ammonia was carried out under a helium flow of 30 ml min^{-1} in the range of 50–500 °C. In a typical CO_2-TPD measurement, 40 mg of sample powder was pretreated for 1 h at 400 °C under a flow of helium at 30 ml min^{-1}. The CO_2 gas flow was introduced after cooling down to 50 °C, followed by purging with helium (30 ml min^{-1}) for 1 h to remove physically adsorbed CO_2. The desorption was carried out under a helium flow of 30 ml min^{-1} in the range of 50–500 °C.

Temperature programmed surface reaction mass spectrometry (TPSR-MS) was conducted using a BELCAT II catalyst analyzer equipped with a mass spectrometer. A 10 mg sample was purged with helium (30 ml min^{-1}) at 400 °C for 1 h and then cooled to 50 °C. Helium (30 ml min^{-1}) was then passed through a cold trap containing 12.1 g of MeOH and 2.1 g of MAc, carrying the saturated vapors of the feedstock through the catalyst bed while the sample was heated up to 700 °C at a rate of 5 °C min^{-1}.

Nitrogen absorption–desorption isotherms were obtained using a Micromeritics 3Flex analyzer. Before measurement, the samples were vacuumed at 200 °C for 4 h to degas the surface. Based on nitrogen absorption–desorption isotherms, the specific surface area was calculated using the Brunauer–Emmett–Teller (BET) method; the pore size distribution was calculated using the Grand Canonical Monte Carlo (GCMC) method.

In situ Fourier transform infrared spectroscopy (*In situ* FTIR) was performed by collecting 64 scans at a resolution of 2 cm^{-1} on a Nicolet Nexus 470 FTIR spectrometer equipped with a liquid-nitrogen-cooled MCT detector. In a typical measurement, about 15 mg of sample powder was pressed into a self-supporting wafer and placed into a cell equipped with ZnSe windows. The samples were pretreated at 400 °C in a He atmosphere at 20 ml min^{-1} for 4 h. Reduction was carried out for 4 h at a flow rate of 20 ml min^{-1} of H_2, followed by purging with N_2 at 20 ml min^{-1} for 30 min. Subsequently, 20 ml per min N_2 passed through a 0 °C cold trap containing 12.1 g MeOH and

2.1 g MAc, carrying the mixture gas into the *in situ* cell while the collection of drift spectra was initiated.

Catalytic performance evaluation

Catalytic performance evaluation for unsaturated ester synthesis was conducted with an 8 mm inner diameter fixed-bed reactor using a designed dual-bed catalyst. First, 200 mg of 40–60 mesh catalyst was loaded into the reactor. Then, a 5 mm layer of quartz wool was filled, followed by filling 200 mg of 40–60 mesh Cs–Al/Q10 catalyst. The reduction process was conducted at 400 °C with 20 mL per min H_2 for 10 h. The reaction was performed at 400 °C with a N_2 flow rate of 20 mL min^{-1}. The nitrogen gas passed through a 0 °C cold trap containing 12.1 g MeOH and 2.1 g MAc. The effluent gas after reaction was analyzed by online gas chromatography (GC) equipped with a capillary column (InertCap 5), which was connected with a flame ionization detector (FID). Conversion of MeOH (C_{MeOH}), MAc (C_{MAC}) and selectivity of products (S_i) based on carbon molar numbers were calculated using the following equations:

$$C_{MeOH}\ (\%) = (A_{MeOH,\ in} - A_{MeOH,\ out})/(A_{MeOH,\ in}) \times 100\%$$
(A is the GC peak area of detected species.)

$$C_{MAc}\ (\%) = (A_{MAc,\ in} - A_{MAc,\ out})/(A_{MAc,\ in}) \times 100\%$$

$$S_i\ (\%) = n_i/\Sigma n_i \times 100\%\ (i = MA, MP, MMA, byproducts;\ n = \text{the amount of substance of i.})$$

Results and discussion

Fig. 2A and B illustrate the XRD patterns of as-synthesized and spent catalysts, providing crucial insights into their structural transformations. The characteristic diffraction peaks at 2θ values of 35.6°, 38.4°, and 38.7°, corresponding to the [−111], [111], and [200] crystal planes of CuO (PDF00-041-0254),[36,37] along with additional peaks at 48.7° [−202], 53.5° [020], 58.4° [202], and 71.6° [−311], confirm the successful dispersion of CuO on the Q10 carrier. Notably, samples 33Cs–22Cu/Q10 and 33Cs/22Cu/Q10, characterized by higher Cu loadings, exhibit enhanced diffraction intensities of CuO, as evidenced by patterns b and f in Fig. 2A. Diffraction peaks at 2θ values of 19.7°

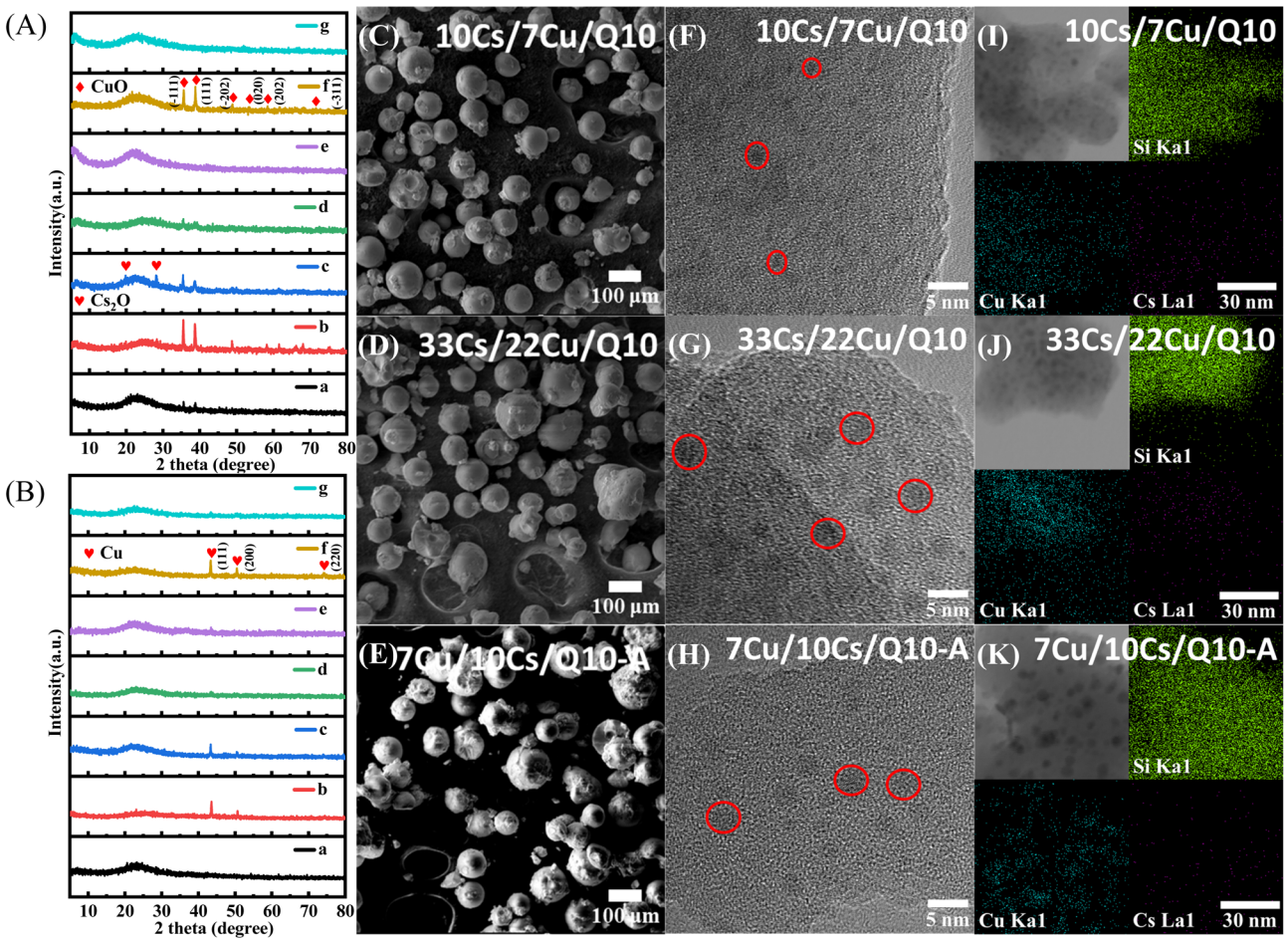

Fig. 2 The XRD patterns of as-synthesized samples (A) and spent samples (B): (a) 10Cs–7Cu/Q10, (b) 33Cs–22Cu/Q10, (c) 7Cu/10Cs/Q10-I, (d) 7Cu/10Cs/Q10-A, (e) 10Cs/7Cu/Q10, (f) 33Cs/22Cu/Q10, and (g) 7Cu/10Cs–Al/Q10; (C)–(E) SEM images of the samples; (F)–(H) HRTEM images of the samples; (I)–(K) EDS mapping analysis of the samples.

and 28.1° indicate the presence of Cs in an oxidized state (Cs_2O) within the as-synthesized catalysts;[38,39] however, their relatively low intensities suggest high dispersion. In contrast, the XRD patterns of spent catalysts reveal a significant transformation: the disappearance of CuO and Cs_2O peaks, replaced by the characteristic peaks of metallic Cu at 2θ values of 43.4° [111], 50.5° [200] and 74.1° [220]. The absence of metallic Cs diffraction peaks implies that the Cs site (Cs_2O) might be covered by coke deposition.

Morphological analysis reveals that all catalysts maintain spherical particle shapes with a diameter of approximately 75 μm. Although the sequential loading of metals does not alter the overall morphology, a notable difference emerges in the particle dispersion. As shown in Fig. S1,† 7Cu/10Cs/Q10-I, prepared *via* double impregnation, exhibits significant particle agglomeration, contrasting sharply with the more dispersed structures of catalysts synthesized by ammonia evaporation (Fig. 2C–E). HRTEM photographs and corresponding EDS surface scanning analysis (Fig. 2F–K) show that CuO and Cs_2O particles are uniformly dispersed on the 10Cs/7Cu/Q10 catalyst, with denser dispersion of these particles observed on the higher metal-loading 33Cs/22Cu/Q10; in contrast, 7Cu/10Cs/Q10-A displays lower Cs energy-dispersive spectroscopy surface scanning density than 10Cs/7Cu/Q10, along with larger metal oxide particles, indicating that the secondary ammonia evaporation treatment causes partial loss of pre-loaded Cs sites and facilitates agglomeration of oxide particles. EDS mapping quantifies the surface loadings of copper and cesium on 10Cs/7Cu/Q10 at 2.1 wt% and 5.3 wt%, respectively, yielding a Cu/Cs mass ratio of 3.96/10 (Fig. S2E†). The catalyst 33Cs/22Cu/Q10, synthesized with increased metal salt inputs, shows substantially higher loadings of 23.3 wt% Cu and 17.2 wt% Cs (Fig. S2F†). The Cu/Cs mass ratio of 4.48/10 on the 7Cu/10Cs/Q10-A catalyst suggests that subsequent metal loading partially covers the sites of the initially loaded metal. Additionally, complementary ICP-OES analysis of the fresh and spent samples (Table S1†) further validates the minimal leaching of Cu, ensuring the stability of the catalytic system.

N_2 adsorption–desorption isotherms (Fig. S3†) and pore size distribution curves (Fig. 3A) provide insights into the catalyst's textural properties. The BET surface areas and average pore diameters are summarized in Fig. 3B. Co-impregnated and multiple impregnated samples retain a consistent mesoporous structure with an average pore size of 14 nm. In contrast,

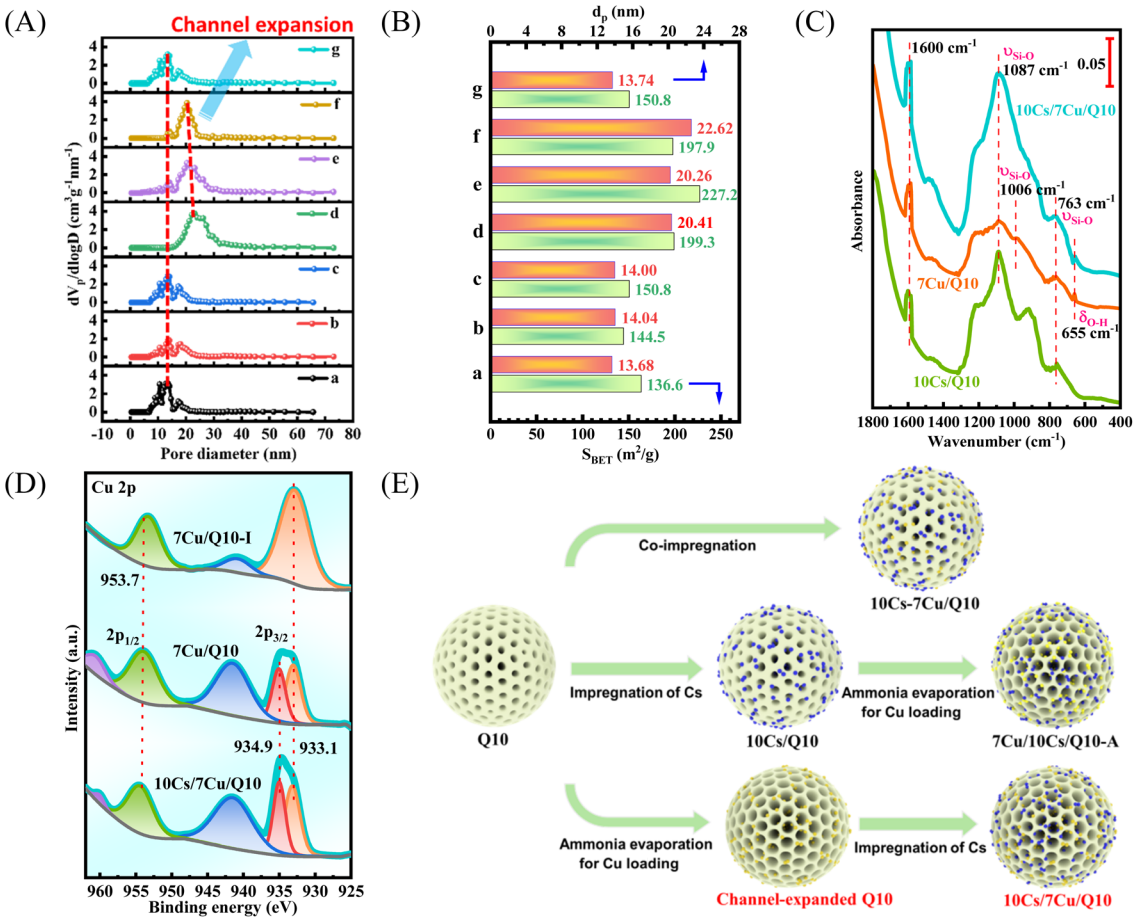

Fig. 3 (A) Calculated GCMC pore size distribution curves of as-synthesized samples. (B) BET surface area and average pore diameter of as-synthesized samples: (a) 10Cs–7Cu/Q10, (b) 33Cs–22Cu/Q10, (c) 7Cu/10Cs/Q10-I, (d) 7Cu/10Cs/Q10-A, (e) 10Cs/7Cu/Q10, (f) 33Cs/22Cu/Q10, and (g) 7Cu/10Cs–Al/Q10. (C) FTIR spectra of 10Cs/Q10, 7Cu/Q10 and 10Cs/7Cu/Q10. (D) Cu 2p XPS spectra of 7Cu/Q10-I, 7Cu/Q10 and 10Cs/7Cu/Q10. (E) Schematic synthesis routes of 10Cs–7Cu/Q10, 7Cu/10Cs/Q10-A, and 10Cs/7Cu/Q10.

ammonia evaporation treatment induces significant structural modifications. Etching of the silica framework creates larger mesopores (20 nm), as indicated by GCMC modeling. These changes also led to a visible extension of the specific surface area of the catalyst from 150 $m^2 g^{-1}$ (7Cu/10Cs/Q10-I) to 200 $m^2 g^{-1}$ (7Cu/10Cs/Q10-A). The enhanced surface area likely improves catalytic activity by exposing more active sites.

FTIR was used to investigate deformations in the silica-oxygen structure of Q10 carriers during the ammonia evaporation process. As depicted in Fig. 3C, absorption bands at 1087 cm^{-1} and 763 cm^{-1} correspond to asymmetric ν_{Si-O} and symmetric ν_{Si-O} stretching vibrations of SiO_2, respectively.[40–47] While bands at 1600 cm^{-1} are associated with physically adsorbed water.[48] These features, originating from Q10 carriers, are readily observable in all tested samples. For 7Cu/Q10, a shoulder peak at 1006 cm^{-1} appears adjacent to the 1087 cm^{-1} bands. This offset asymmetric ν_{Si-O} stretching vibration originates from copper phyllosilicate ($Cu_2Si_2O_5(OH)_2$). The absorption bands at 655 cm^{-1} indicate bending vibration of the hydroxyl group δ_{O-H} in copper phyllosilicate.[40–42] The shoulder peak around 1006 cm^{-1} is less pronounced in 10Cs/7Cu/Q10, suggesting that subsequent Cs loading weakens the Si–O vibrational signal in copper phyllosilicate *via* the formation of Si–O–Cs linkages. However, the absorption bands of the characteristic bending vibrations δ_{OH} (655 cm^{-1}) remain clearly visible.

XPS analysis (Fig. 3D and S4†) provides further evidence for copper phyllosilicate formation. For CuO, the Cu $2p_{1/2}$ and Cu $2p_{3/2}$ binding energies typically appear at 954 eV and 933 eV, respectively.[34,41] In 7Cu/Q10-I prepared by impregnation, peaks at 953.7 eV and 933.1 eV confirm the presence of surface CuO. A significant shift in the Cu $2p_{3/2}$ binding energy to 934.9 eV was observed over the catalysts prepared by the ammonia evaporation method (7Cu/Q10 and 10Cs/7Cu/Q10). This shift is characteristic of Cu 2p in copper phyllosilicate.[40] Additionally, the Cu^{2+} satellite peaks in the XPS spectra of all samples within the range of 940–945 eV confirmed the d^9 electronic configuration of Cu ions.[41] In the Cs 3d region of 10Cs/7Cu/Q10 (Fig. S4B†), peaks at binding energies of 725.5 eV (Cs $3d_{5/2}$) and 739.6 eV (Cs $3d_{3/2}$) indicate the presence of Cs_2O.[39,49,50]

These findings elucidate the molecular mechanism of channel-expanding effect by the ammonia evaporation method. As illustrated in Fig. 3E, co-impregnation deposits metals primarily on the external surface and within narrow pores. In contrast, ammonia solutions containing copper–ammonia complexes etch the silica framework by forming copper phyllosilicate. This process enlarges the original 14 nm mesopores to 20 nm, and the larger mesopores result in an extension of specific surface area. The expanded pores facilitate uniform metal dispersion and enhance mass transfer. After Q10 is pretreated with copper nitrate and ammonia, subsequent Cs species disperse more effectively within the enlarged mesopores. Impregnation methods without prior pore expansion lead to preferential Cs deposition on the catalyst surface.

To probe the activity enhancement benefits from the channel-expanding strategy, the catalytic performance of two series of catalysts—10Cs–7Cu/Q10 and 33Cs–22Cu/Q10 (co-impregnation) *vs.* 10Cs/7Cu/Q10 and 33Cs/22Cu/Q10 (ammonia evaporation)—was evaluated for one-step unsaturated ester synthesis. As shown in Fig. 4A, 10Cs–7Cu/Q10 achieved 35.9% MeOH conversion and 52.6% MAc conversion, with MA and MP selectivities of 48.8% and 4.8%, respectively (Fig. 4E). Tripling the metal loading (33Cs–22Cu/Q10) reduced MAc conversion to 35.3% (Fig. 4B), implying that the excessive metal loading decreases active site accessibility. Narrow pores and metal stacking likely impede reactant diffusion, leading to increased by-products (*e.g.*, 2-methacrolein, methyl isobutyrate and propionaldehyde) and lower selectivity of MA (38.4%). In contrast, the channel-expanding catalyst 10Cs/7Cu/Q10 significantly improved both MeOH (55.3%) and MAc (59.8%) conversion (Fig. 4C). MA selectivity increased to 59.2%, accompanied by 5.3% MMA formation *via* the further condensation of MP and formaldehyde. In contrast to catalysts prepared by the co-impregnation method, when increasing the metal loading on

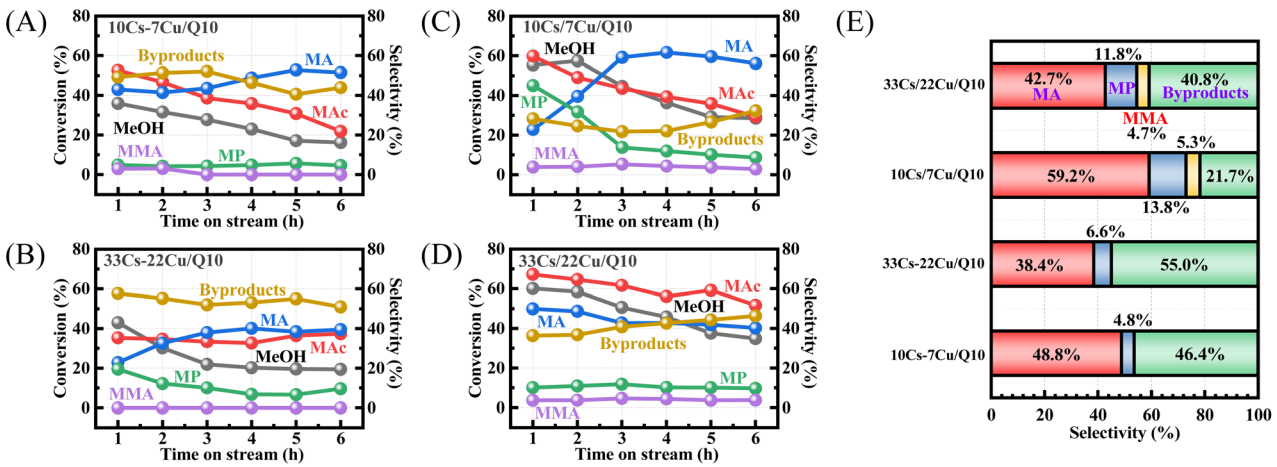

Fig. 4 Catalytic performance of (A) 10Cs–7Cu/Q10, (B) 33Cs–22Cu/Q10, (C) 10Cs/7Cu/Q10, and (D) 33Cs/22Cu/Q10. (E) Product selectivity over different samples. Reaction conditions: dual layer catalytic bed with 0.2 g sample loaded in the upper layer and 0.2 g Cs–Al/Q10 in the lower layer, GHSV = 3000 ml $g^{-1} h^{-1}$, 400 °C, 0.1 MPa, MeOH/MAc = 2/1, N_2 flow rate 20 mL min^{-1}.

33Cs/22Cu/Q10, it was found that the conversions of MeOH and MAc increased to 60.1% and 67.2%, respectively. This implies that 33Cs–22Cu/Q10, which means the channel-expanding strategy mitigates metal stacking and enhances catalytic performance.

In situ FTIR was employed to monitor surface changes during reduction and reaction (Fig. 5 and S5†). During the 2 h reduction of 7Cu/Q10 (Fig. 5A), a broad inverse absorption band near 3600–3300 cm^{-1} was assigned to O–H stretching vibrations of water absorbed on the surface of CuO.[51,52] This band was absent in 10Cs/Q10 during the same reduction process (Fig. 5B), confirming that the water originated from CuO surfaces. As H_2 reduced CuO to metallic Cu, adsorbed H_2O desorbed, explaining the band's decline. For the same reason, a similar band around 3200 cm^{-1} appeared during the reduction of 10Cs/7Cu/Q10 (Fig. 5C). Sharp bands at 2367 cm^{-1} and 2337 cm^{-1} in Fig. 5A were assigned to CO_2 infrared signatures.[53,54]

Surface information of 7Cu/Q10 was also recorded under the atmosphere of MeOH/MAc mixtures to model the reaction process. A sharp negative band at 3744 cm^{-1} corresponded to O–H stretching vibration of isolated silanol groups (Fig. 5D),[55–57] arising from hydrogen bonding between MeOH and silanol groups. This interaction was negligible on the 10Cs/Q10 surface (Fig. 5E), indicating that MeOH preferentially adsorbs on Cu rather than Cs sites. Bands at 2953 cm^{-1} and 2854 cm^{-1} correspond to C–H asymmetric/symmetric vibrations of $*CH_3$ species in MeOH/MAc.[57–59] The absorption bands at 1765 cm^{-1} and 1240 cm^{-1} corresponded to the C=O symmetric stretching vibration and C–O stretching mode of $*COOCH_3$ species in MAc, respectively.[60–66] Another 1053 cm^{-1} absorption band indicated C–O stretching mode in MeOH.[67,68]

For 10Cs/Q10 (Fig. 5E), apart from characteristic peaks of MeOH and MAc (absorption bands at 2953 cm^{-1}, 2854 cm^{-1}, 1765 cm^{-1}, 1240 cm^{-1} and 1053 cm^{-1}), a 1583 cm^{-1} characteristic band revealed C=C symmetric stretching vibration,[69,70] indicating solid evidence for the formation of unsaturated esters (MA and MMA). This implies that aldol condensation occurs at Cs sites.[49,71–75] It is hypothesized that Cs-driven activation of MAc's carbonyl group enables enolate formation even without formaldehyde substitution. The absence of C=C bands on 7Cu/Q10 confirms that Cs sites are critical for condensation.

As shown in Fig. 5F, the more pronounced absorption band at 3744 cm^{-1} indicated enhanced MeOH adsorption and conversion on 10Cs/7Cu/Q10 compared to 7Cu/Q10. While MeOH and MAc signals persisted (2953 cm^{-1}, 2854 cm^{-1}, 1765 cm^{-1}, 1240 cm^{-1} and 1053 cm^{-1}), it is noteworthy that the 1583 cm^{-1} band (C=C) was more intense than that of 1765 cm^{-1} (C=O), contrasting with 10Cs/Q10. This stems from DED synergy: Cu-engine promotes the conversion of MeOH to formaldehyde, which provides the feedstock for aldol condensation, while protons (*H) produced by the above process can reduce unsaturated MA to MP, enabling subsequent condensation with formaldehyde to obtain more MMA.

The catalytic performance of 10Cu/Q10 and 7Cs/Q10 (Fig. S6†) is consistent with the infrared conclusions: in the Cu-only system, MeOH conversion remains at 27%, while MAc conversion is below 2%. This confirms that Cu promotes MeOH conversion, but MAc activation is negligible without the Cs-engine. Formaldehyde was the main by-product without any ester generation. In the Cu-only system, MeOH conversion is only 5% (lacking Cu-engine), and MAc conversion is 2–3%, significantly lower than the 30–60% observed on the DED catalyst (10Cs/7Cu/Q10). Under formaldehyde-deficient conditions, Cs-engine alone cannot facilitate efficient aldol condensation of MAc with formaldehyde. Trace MA was detected, but no MP was observed, indicating that proton availability for MA

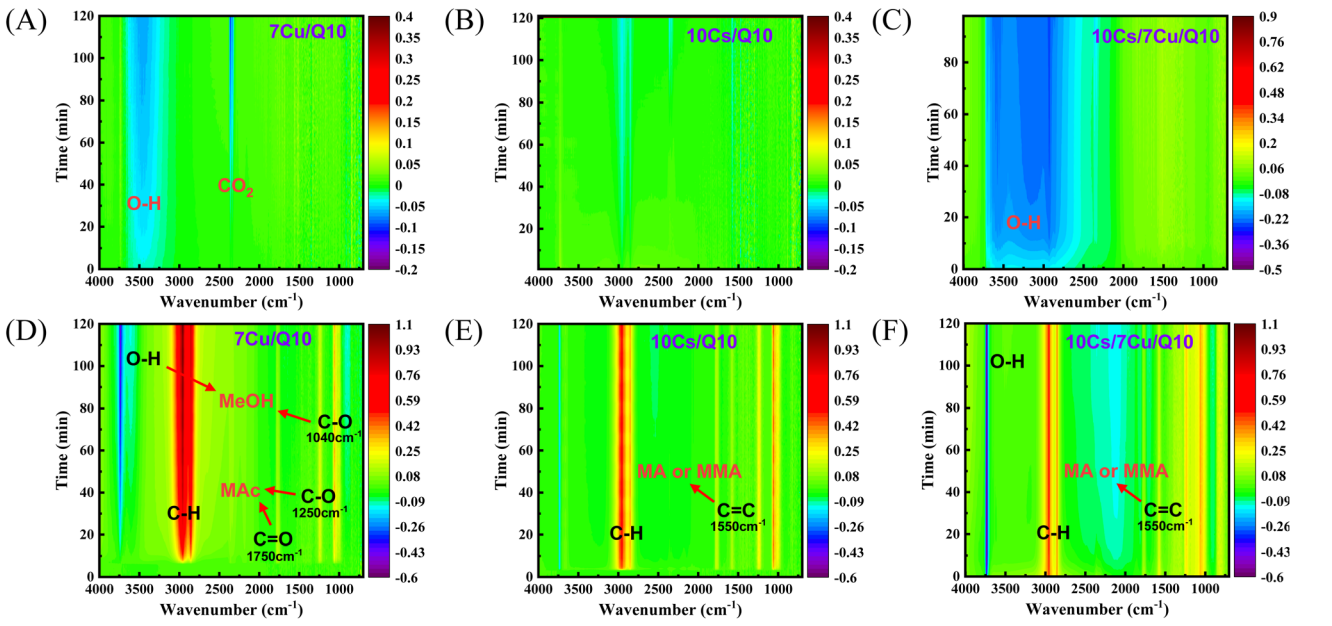

Fig. 5 *In situ* FTIR spectra of as-synthesized samples during reduction and reaction: reduction of 7Cu/Q10 (A), 10Cs/Q10 (B), and 10Cs/7Cu/Q10 (C); reaction over 7Cu/Q10 (D), 10Cs/Q10 (E), and 10Cs/7Cu/Q10 (F).

hydrogenation is insufficient without Cu-driven dehydrogenation.

These findings underscore the synergistic interplay between Cu and Cs in the DED catalyst: Cu facilitates MeOH dehydrogenation to generate formaldehyde and protons, while Cs activates MAc *via* carbonyl coordination, enabling efficient aldol condensation. The presumed reaction pathway (Fig. 6), based on *in situ* FTIR analysis, proceeds as follows: firstly, MeOH is dehydrogenated on Cu sites to produce formaldehyde, which is activated to a carbon cation immediately. Simultaneously, Cs coordinates the carbonyl group of MAc, enhancing α-carbon nucleophilicity. Aldol condensation between these activated species yields a hydroxyl intermediate and the unstable intermediate, which dehydrates to form the primary unsaturated ester MA. Secondly, MA is hydrogenated to the saturated ester MP using protons derived from MeOH dehydrogenation, mediated by Cu sites. This step highlights the dual role of the Cu-engine in both formaldehyde generation and subsequent hydrogenation. Thirdly, Cs coordinates the carbonyl group of MP, enabling Cu-driven α-hydrogen abstraction to form a nucleophilic carbanion. Electrophilic substitution with activated formaldehyde generates a secondary intermediate, which undergoes dehydration to yield MMA. Protons released during this step recombine as H_2 gas. The exclusive α-carbon substitution in unsaturated esters arises from Cs-driven carbonyl polarization, which directs electrophilic substitution to the α-carbon position. This mechanistic insight demonstrates the cooperative roles of Cu (redox) and Cs (base) in enabling the sequential dehydrogenation, condensation, and hydrogenation steps that are critical for efficient MMA synthesis.

Given the critical role of acidity and alkalinity in activating formaldehyde as well as MAc, NH_3-TPD and CO_2-TPD were conducted to characterize the acid–base properties of the samples (Fig. 7A, B and S7†). Desorption peaks appearing at 50–150 °C are attributed to weak acid and base sites, those at 150–300 °C to medium sites, and signals at 300 to 500 °C are summarized as strong acid and base sites.

Vertical peak integration (Fig. 7C) showed that 10Cs/7Cu/Q10 possessed 302 μmol NH_3 per g total acid sites, primarily weak (121 μmol NH_3 per g) and medium acids (162 μmol NH_3 per g), along with comparable weak (97 μmol CO_2 per g) and medium (123 μmol CO_2 per g) base sites. As expected, 33Cs/22Cu/Q10 exhibited higher acid (433 μmol NH_3 per g) and base site (314 μmol CO_2 per g) densities. These acid and base sites originate from the loaded Cu and Cs elements and linearly correlate with their content. Adjusting the Cu/Cs ratio revealed that increase in Cu loading enhanced weak acids (121 μmol NH_3 per g in 7Cs/10Cu/Q10), while higher Cs loading enriched medium base sites (151 μmol CO_2 per g in 13Cs/4Cu/Q10). Comparing 10Cs/7Cu/Q10 (Fig. 4C) and 13Cs/4Cu/Q10 (Fig. 7D) at close MAc conversions (60%), the latter showed improved MA selectivity in the first 2 h. It highlights the contribution of the Cs-engine in aldol condensation since the extra Cs promotes the MAc conversion. However, the proton transfer between MeOH and MA was limited because of the insufficient Cu-engine, reducing the conversion of MeOH and selectivity of MP (3.1%). For 7Cs/10Cu/Q10 (Fig. 7E), MeOH/MAc conversions were 38.3% and 47.5%, respectively. Despite the guaranteed amount of Cu loading, reduced MeOH conversion stemmed from insufficient Cs-driven MA activation, while

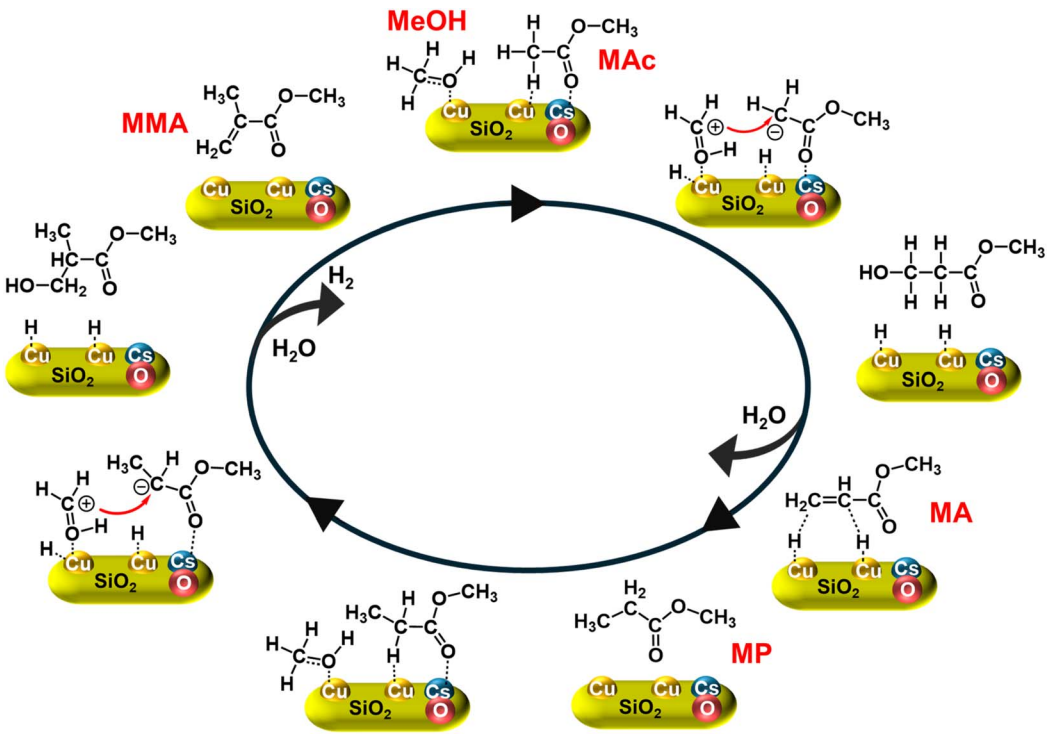

Fig. 6 Presumed reaction pathway for DED synthesis of unsaturated esters over the Cu–Cs catalyst.

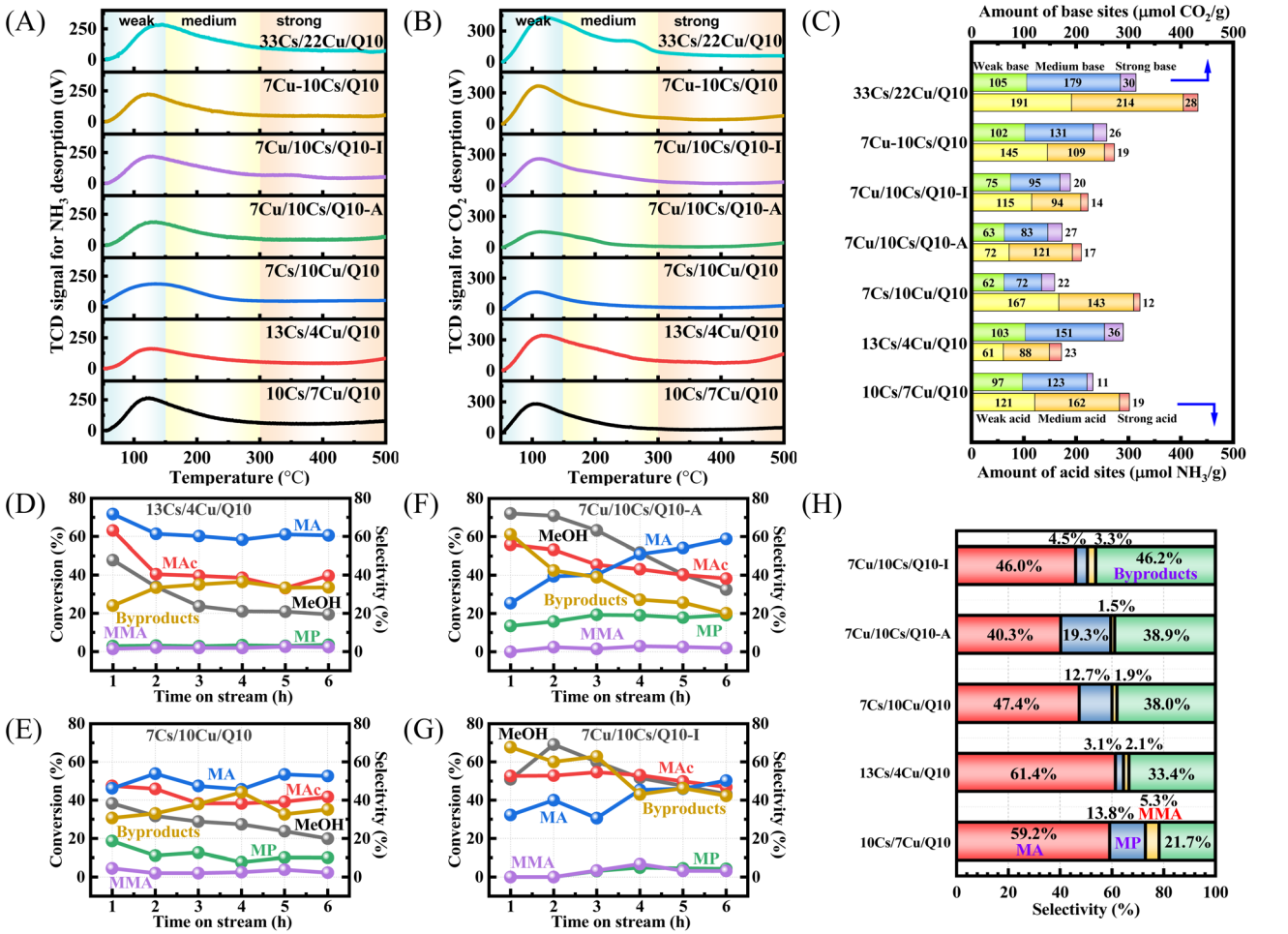

Fig. 7 (A) NH_3-TPD profiles of as-synthesized samples; (B) CO_2-TPD profiles of as-synthesized samples; (C) amounts of acid and base sites determined by NH_3-TPD and CO_2-TPD; catalytic performance of (D) 13Cs/4Cu/Q10, (E) 7Cs/10Cu/Q10, (F) 7Cu/10Cu/Q10-A, and (G) 7Cu/10Cs/Q10-I. (H) Product selectivity over different samples. Reaction conditions: dual layer catalytic bed with 0.2 g sample loaded in the upper layer and 0.2 g Cs–Al/Q10 in the lower layer, GHSV = 3000 ml g^{-1} h^{-1}, 400 °C, 0.1 MPa, MeOH/MAc = 2/1, N_2 flow rate 20 mL min^{-1}.

12.7% selectivity of MP indicated near-saturation of proton acceptance by MA. These results confirm that the Cu and Cs engines act synergistically rather than independently to promote the generation of MA and MMA. Catalysts with reversed metal loading order (7Cu/10Cs/Q10-A and 7Cu/10Cs/Q10-I) exhibited lower amounts of acid sites and base sites (210 μmol NH_3 per g, 173 μmol CO_2 per g *vs.* 223 μmol NH_3 per g, 190 μmol CO_2 per g, respectively). The production over 7Cu/10Cs/Q10-A contains 19.3% MP probably due to a higher amount of medium acid sites (121 μmol NH_3 per g), while 46.2% of by-products were generated on 7Cu/10Cs/Q10-I because of imbalanced acid–base ratios. In contrast, 10Cs/7Cu/Q10's optimal acid–base ratio and a higher percentage of medium acid and medium base, enabled superior catalytic performance.

Notably, Cs–Al/Q10 was introduced as a second catalyst bed in a series of previously executed reactions to enhance the formation of unsaturated esters, as it promotes the condensation of MP with formaldehyde and accelerates the consumption of MAc and excess formaldehyde according to the previous reports.[34,76] Here we investigated the role of the lower Cs–Al/Q10 bed through comparative experiments with or without its loading, using Cu-loaded Cs–Al/Q10 as a reference (Fig. 8E). With dual-bed catalysts (Fig. 8B), the selectivity of MA increased from 21% at 1 h to a stable 59%, whereas the single-bed system without Cs–Al/Q10 showed only 5% MA selectivity at 1 h (Fig. 8D), with 43% MP and 48% byproducts. This confirms that Cs–Al/Q10 preferentially drives MAc to MA rather than to by-products.

In the dual-bed system (10Cs/7Cu/Q10 + Cs–Al/Q10), the selectivity of the saturated ester MP initially reached 45% but decreased to 15% as the reaction proceeded, compared to 30.3% MP selectivity in the single-bed system (Fig. 8G). This indicates that Cs–Al/Q10 accelerates the condensation of MP to MMA, evidenced by the MMA selectivity enhancement by adding Cs–Al/Q10 (from 4.9% to 5.3%). Conversely, 7Cu/10Cs–Al/Q10 (Fig. 8F) showed 38.3% MeOH and 47.5% MAc conversion without MMA formation, suggesting that Cu loading on Cs–Al/Q10 limits Cs-driven MAc/MP activation. Dual-bed configuration optimizes Cu/Cs site utilization.

TPSR-MS analysis (Fig. 8H–K) probed the reaction dynamics with or without Cs–Al/Q10, and fragment m/z values for relevant chemicals are given in Table S2.† $^*CH_3$ (m/z = 31) fragments

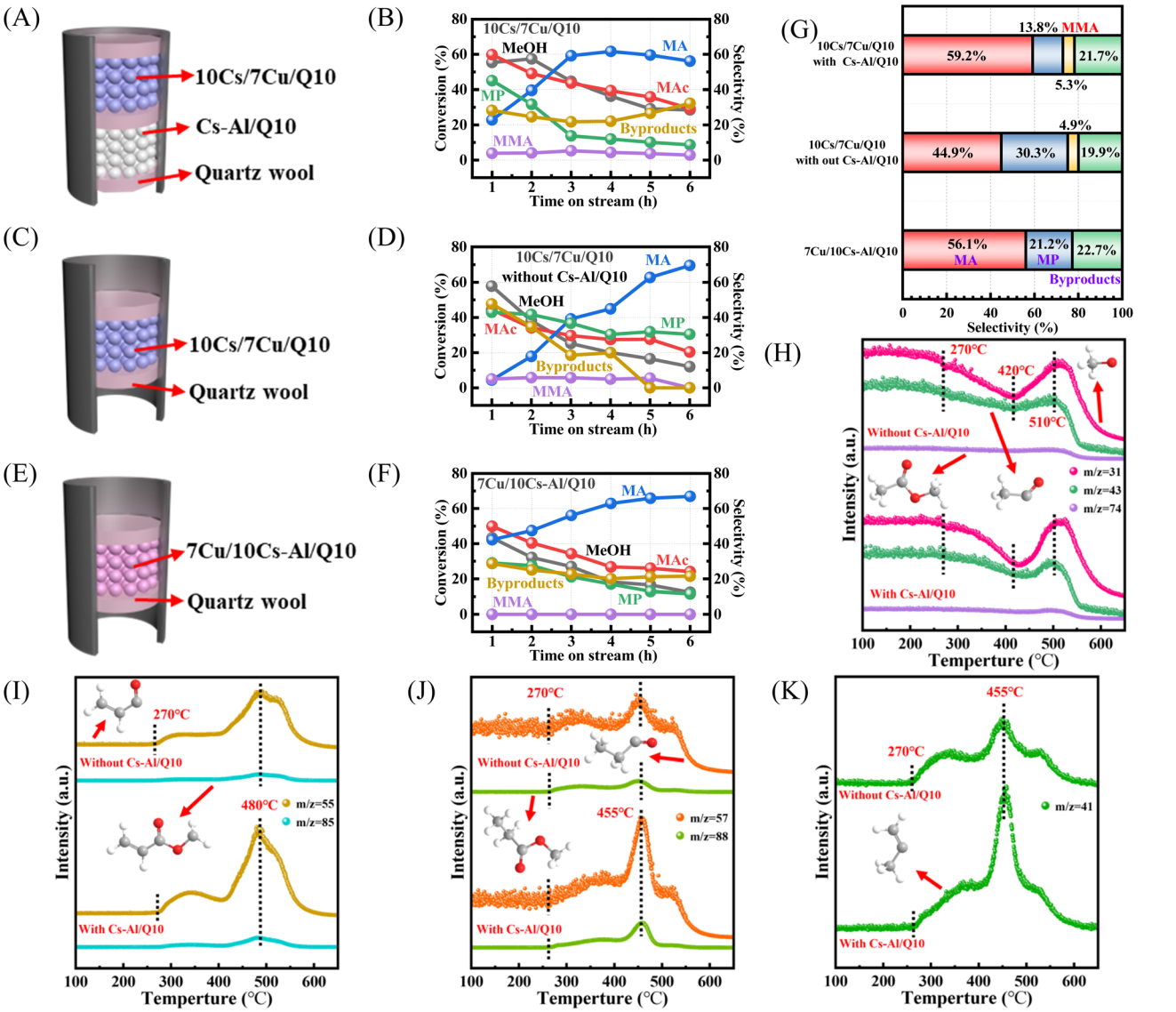

Fig. 8 Catalyst bed loading strategies and catalytic performance of (A and B) 10Cs/7Cu/Q10 with Cs–Al/Q10; (C and D) 10Cs/7Cu/Q10 without Cs–Al/Q10; (E and F) 7Cu/10Cs–Al/Q10. (G) Product selectivity over different samples. TPSR-MS profiles of 10Cs/7Cu/Q10 with Cs–Al/Q10 and 10Cs/7Cu/Q10 without Cs–Al/Q10: (H) signals of MeOH and MAc; (I) signals of MA; (J) signals of MP; (K) signals of MMA.

represent MeOH, while *$COCH_3$ ($m/z = 43$) fragments as well as MAc molecular fragments ($m/z = 74$) represent MAc. These signals decreased from 270 °C, reaching a minimum at 420 °C, indicating vigorous reaction between MeOH and MAc at this temperature. A rebound in fragment intensity above 510 °C suggested side reactions.

Among the product fragments, *$COCH{=}CH_2$ ($m/z = 55$) and the MA molecule ($m/z = 85$) fragments peaked at 480 °C,[77] while *$COCH_2CH_3$ ($m/z = 57$) fragments and MP molecule ($m/z = 88$) fragments showed maximum signals at 455 °C. The decline in MP signals and rise in MA signals between 455 to 480 °C indicate that the hydrogenation of MA favors lower temperatures, consistent with theoretical calculations.[78] The fragments with $m/z = 41$ representing *$C(CH_3){=}CH_2$, corresponding to MMA, also peaked at 455 °C, overlapping with MP signals, reflecting abundant formaldehyde in the reaction system. All product fragment intensities were higher in the dual-bed system, reconfirming Cs–Al/Q10's role in the acceleration of MP condensation.

A 24-hour stability test was conducted using the optimal 10Cs/7Cu/Q10 catalyst in the unsaturated ester synthesis system on a dual-layer catalytic bed (Fig. S8†). The results show that the selectivity of MA remains relatively stable over TOS, while the selectivities of MP and MMA decrease gradually. The selectivity of byproducts increases slightly during the test period, and starting from the 12th hour, the conversion of MAc shows a gradual decline. Overall, the 10Cs/7Cu/Q10 catalyst demonstrates good stability in this synthesis system, indicating its potential for practical applications in the one-step synthesis of unsaturated esters.

Conclusions

In this study, a DED catalytic system was developed for the one-step synthesis of unsaturated ester from MeOH and MAc. The designed catalyst integrates a Cu-engine and a Cs-engine, addressing the critical challenge of spatiotemporal mismatch in proton transfer during MeOH dehydrogenation and MA hydrogenation. The Cu-engine facilitates proton shuttling to synchronize these two reactions macroscopically, while the Cs-engine, acting as base sites, activates the α-carbon of the saturated esters (MAc and MP) by carbonyl coordination, enabling efficient aldol condensation with formaldehyde. This dual functionality provides a seamless, synergistic mechanism for the entire reaction network. As evidenced by *in situ* FTIR, the absence of C=C absorption bands over the single Cu-engine catalyst ($7Cu/SiO_2$) confirms the indispensable role of Cs for unsaturated ester formation. In contrast, the DED catalyst (10Cs/7Cu/Q10) exhibited enhanced MeOH adsorption and product signals compared to the Cs-only (10Cs/Q10) system.

Additionally, an ammonia evaporation method introduced a channel-expanding strategy during catalyst preparation. Compared to the co-impregnated 10Cs–7Cu/Q10, 10Cs/7Cu/Q10 showed a 50% increase in average pore diameter and a 60% expansion in specific surface area. In a dual-bed catalytic system combining Cs–Al/Q10, the overall selectivity of unsaturated esters reached 64.5%. The present work achieves the efficient synthesis of unsaturated esters *via* a channel-expanding Cu–Cs DED catalyst, offering a new paradigm for catalyst design and modification in multi-step transformations.

Data availability

The data supporting this article have been included as part of the ESI.†

Author contributions

J. F. and L. S.: data curation, formal analysis, methodology, writing – original draft. W. G. and Y. H.: data curation. W. X., H. H. and Z. L.: formal analysis. C. L. and B. W.: visualization. K. W. and G. L.: validation. J. S., Q. L., T. L., T. X. and S. Y.: resources. Z. Y., G. Y., P. Z. and N. T.: supervision, conceptualization, writing – review and editing. All the authors contributed to the discussions on the results.

Conflicts of interest

There are no conflicts to declare.

Acknowledgements

We appreciate the financial assistance from JST SPRING, Grant Number JPMJSP2145, the Science and Technology Innovation Program of Hunan Province (2024RC3195), the Research Foundation of Education Bureau of Hunan Province (23B0241), and the Nature Science Foundation of Hunan Province (2025JJ50095).

Notes and references

1 K. Nollenberger and J. Albers, Poly(meth)acrylate-based coatings, *Int. J. Pharm.*, 2013, **457**, 461–469.
2 Z. A. A. Latif, A. M. Mohammed and N. M. Abbass, Synthesis and characterization of polymer nanocomposites from methyl acrylate and metal chloride and their application, *Polym. Bull.*, 2020, **77**, 5879–5898.
3 W. Li, Y. Wu, Z. Xu, Q. Ni, J. Xing and X. Tao, Blending caproylated starch with poly(acrylic acid)-g-protein-g-poly(methyl acrylate) as an adhesive material to improve the adhesion of starch to PLA fibers, *Int. J. Adhes. Adhes.*, 2020, **102**, 102668.
4 S. Salaeh, S. Nobnop, B. Thongnuanchan, A. Das and S. Wießner, Thermo-responsive programmable shape memory polymer based on amidation cured natural rubber grafted with poly(methyl methacrylate), *Polymer*, 2022, **262**, 125444.
5 L. Hentschel, F. Kynast, S. Petersmann, C. Holzer and J. Gonzalez-Gutierrez, Processing Conditions of a Medical Grade Poly(Methyl Methacrylate) with the Arburg Plastic Freeforming Additive Manufacturing Process, *Polymers*, 2020, **12**, 2677.
6 Z. Saki, I. D'Auria, A. Dall'Anese, B. Milani and C. Pellecchia, Copolymerization of Ethylene and Methyl Acrylate by Pyridylimino Ni(II) Catalysts Affording Hyperbranched Poly(ethylene-co-methyl acrylate)s with Tunable Structures of the Ester Groups, *Macromolecules*, 2020, **53**, 9294–9305.
7 L. Cao, Z. Cai and M. Li, Phosphinobenzenamine Nickel Catalyzed Efficient Copolymerization of Methyl Acrylate with Ethylene and Norbornene, *Macromolecules*, 2022, **55**, 3513–3521.
8 K. Nagai, New developments in the production of methyl methacrylate, *Appl. Catal., A*, 2001, **221**, 367–377.
9 F. Fixe, M. Dufva, P. Telleman and C. B. V. Christensen, Functionalization of poly(methyl methacrylate) (PMMA) as a substrate for DNA microarrays, *Nucleic Acids Res.*, 2004, **32**, e9.
10 U. Ali, K. J. B. A. Karim and N. A. Buang, A Review of the Properties and Applications of Poly (Methyl Methacrylate) (PMMA), *Poly. Rev.*, 2015, **55**, 678–705.
11 G. Hayes, M. Laurel, D. MacKinnon, T. Zhao, H. A. Houck and C. R. Becer, Polymers without Petrochemicals: Sustainable Routes to Conventional Monomers, *Chem. Rev.*, 2023, **123**, 2609–2734.
12 A. A. Adeoye, F. Passarini, J. De Maron, T. Tabanelli, F. Cavani and D. Cespi, Methyl Methacrylate Production Processes: A Comparative Analysis of Alternatives Using the Life Cycle Assessment Methodology, *ACS Sustain. Chem. Eng.*, 2023, **11**, 17355–17370.
13 M. J. Darabi Mahboub, J.-L. Dubois, F. Cavani, M. Rostamizadeh and G. S. Patience, Catalysis for the synthesis of methacrylic acid and methyl methacrylate, *Chem. Soc. Rev.*, 2018, **47**, 7703–7738.
14 J. Li, H. Li, Z. Liu, M. Akri, Y. Tan, L. Kang, J. Chi, B. Qiao and Y. Ding, Synergic effect between gold and vanadate

substituted hydroxyapatite support for synthesis of methyl methacrylate by one-step oxidative esterification, *Chem. Eng. J.*, 2022, **431**, 133207.
15 Y. Zhang, X. Cui, F. Shi and Y. Deng, Nano-Gold Catalysis in Fine Chemical Synthesis, *Chem. Rev.*, 2012, **112**, 2467–2505.
16 M. U. Farooq, Y. Shi, W. Chen, Y. Guan, J. Zhou, N. Song, G. Qian, J. Zhang, D. Chen, X. Zhou and X. Duan, Kinetics insights into the active sites of Au catalysts for the oxidative esterification of methacrolein to methyl methacrylate, *Chem. Eng. Sci.*, 2023, **277**, 118840.
17 M. U. Farooq, R. R. Zairov, B. Arkook, M. Harb and M. M. Makhlouf, Gold nanocatalysts supported on Mono-/Mixed oxides for efficient synthesis of methyl methacrylate, *Fuel*, 2025, **382**, 133763.
18 L. Wang, Y. Bian, Z. Wu, Z. Li, G. Wang and C. Li, Revealing the role of hydrogen bond, mechanism and kinetic for hydroesterification of ethylene to methyl propionate, *Chem. Eng. J.*, 2023, **470**, 144331.
19 L. Wang, Z. Li, E. Wang and C. Li, The effect of ligand and acid promoter on hydroesterification of ethylene to methyl propionate and kinetic studies, *Mol. Catal.*, 2022, **533**, 112746.
20 L. Xu, X. Wang, J. Song, J. Liu and D. Liu, Acid Promoter-Modified Cs/Al2O3 Catalyst for Methyl Methacrylate Production by Aldol Condensation of Methyl Propionate with Formaldehyde, *Ind. Eng. Chem. Res.*, 2023, **62**, 21130–21139.
21 L. Shi, W. Shen, G. Yang, X. Fan, Y. Jin, C. Zeng, K. Matsuda and N. Tsubaki, Formic acid directly assisted solid-state synthesis of metallic catalysts without further reduction: As-prepared Cu/ZnO catalysts for low-temperature methanol synthesis, *J. Catal.*, 2013, **302**, 83–90.
22 G. Liu, H. Hagelin-Weaver and B. Welt, A Concise Review of Catalytic Synthesis of Methanol from Synthesis Gas, *Waste*, 2023, **1**, 228–248.
23 D. Laudenschleger, H. Ruland and M. Muhler, Identifying the nature of the active sites in methanol synthesis over Cu/ZnO/Al2O3 catalysts, *Nat. Commun.*, 2020, **11**, 3898.
24 X. Jiang, W. Yang, H. Song, J. Ke, P. Li, R. Li, Q. Ma, J. Sun, T.-S. Zhao and N. Tsubaki, Effect of glucose pretreatment on Cu–ZnO–Al2O3 catalyzed CO2 hydrogenation to methanol, *RSC Adv.*, 2023, **13**, 22493–22502.
25 P. Li, J. Bi, J. Liu, Q. Zhu, C. Chen, X. Sun, J. Zhang and B. Han, In situ dual doping for constructing efficient CO2-to-methanol electrocatalysts, *Nat. Commun.*, 2022, **13**, 1965.
26 K. Natte, H. Neumann, M. Beller and R. V. Jagadeesh, Transition-Metal-Catalyzed Utilization of Methanol as a C1 Source in Organic Synthesis, *Angew. Chem., Int. Ed.*, 2017, **56**, 6384–6394.
27 G. Choi and S. H. Hong, Selective Monomethylation of Amines with Methanol as the C1 Source, *Angew. Chem., Int. Ed.*, 2018, **57**, 6166–6170.
28 Y.-M. Wang, J.-B. Wang, J. Huang, Z.-S. Cui, M. Zhang and Z.-H. Zhang, Molybdenum disulfide-catalyzed direct α-hydroxymethylation of amides employing methanol as a sustainable C1 source under photoirradiation, *J. Catal.*, 2023, **427**, 115100.
29 G. Wang, Z. Li, C. Li and S. Zhang, Preparation of methyl acrylate from methyl acetate and methanol with mild catalysis of cobalt complex, *Chem. Eng. J.*, 2019, **359**, 863–873.
30 G. Wang, X. Hu and S. Zhao, Kinetic and thermodynamic studies on direct synthesis of methyl methacrylate from methyl propionate and methanol catalyzed by highly efficient cobalt complex at mild conditions, *Chem. Eng. J.*, 2023, **468**, 143592.
31 A. Trimpalis, G. Giannakakis, S. Cao and M. Flytzani-Stephanopoulos, NiAu single atom alloys for the selective oxidation of methacrolein with methanol to methyl methacrylate, *Catal. Today*, 2020, **355**, 804–814.
32 B. Wang, Z. Luo, Q. Qin, H. Dong and H. Liu, Effect of the coverage of modulated Au(Pd) atoms over bimetallic Pd-Au catalysts on catalytic performance for direct oxidative esterification of methacrolein into methyl methacrylate, *Mol. Catal.*, 2021, **514**, 111783.
33 Z. Wu, L. Wang, Z. Li, G. Wang and C. Li, Unveiling the promotion of Brønsted acid sites in Cs dispersion and consequential Si-O-Cs species formation for methyl acrylate synthesis from methyl acetate and formaldehyde over Cs/Beta zeolite catalyst, *Chem. Eng. J.*, 2023, **474**, 145655.
34 W. Chen, J. Zuo, K. Sang, G. Qian, J. Zhang, D. Chen, X. Zhou, W. Yuan and X. Duan, Leveraging the Proximity and Distribution of Cu–Cs Sites for Direct Conversion of Methanol to Esters/Aldehydes, *Angew. Chem., Int. Ed.*, 2023, **63**, e202314288.
35 X. Wu, C. Wang, S. Zhao, Y. Wang, T. Zhang, J. Yao, W. Gao, B. Zhang, T. Arakawa, Y. He, F. Chen, M. Tan, G. Yang and N. Tsubaki, Dual-engine-driven realizing high-yield synthesis of Para-Xylene directly from CO2-containing syngas, *Nat. Commun.*, 2024, **15**, 8064.
36 M. Bin Mobarak, M. S. Hossain, F. Chowdhury and S. Ahmed, Synthesis and characterization of CuO nanoparticles utilizing waste fish scale and exploitation of XRD peak profile analysis for approximating the structural parameters, *Arabian Journal of Chemistry*, 2022, **15**, 104117.
37 C. S. Philip, A. Nivetha, C. Sakthivel, C. G. Veena and I. Prabha, Novel fabrication of cellulose sprinkled crystalline nanocomposites using economical fibrous sources: High performance, compatible catalytic and electrochemical properties, *Microporous Mesoporous Mater.*, 2021, **318**, 111021.
38 H. M. A. Hassan, M. S. Alhumaimess, I. H. Alsohaimi, A. A. Essawy, M. F. Hussein, H. M. Alshammari and O. F. Aldosari, Biogenic-Mediated Synthesis of the Cs2O–MgO/MPC Nanocomposite for Biodiesel Production from Olive Oil, *ACS Omega*, 2020, **5**, 27811–27822.
39 G. Zhang, H. Zhang, D. Yang, C. Li, Z. Peng and S. Zhang, Catalysts, kinetics and process optimization for the synthesis of methyl acrylate over Cs–P/γ-Al2O3, *Catal. Sci. Technol.*, 2016, **6**, 6417–6430.
40 F. Li, L. Wang, X. Han, Y. Cao, P. He and H. Li, Selective hydrogenation of ethylene carbonate to methanol and ethylene glycol over Cu/SiO2 catalysts prepared by

ammonia evaporation method, *Int. J. Hydrogen Energy*, 2017, **42**, 2144–2156.

41 L.-F. Chen, P.-J. Guo, M.-H. Qiao, S.-R. Yan, H.-X. Li, W. Shen, H.-L. Xu and K.-N. Fan, Cu/SiO2 catalysts prepared by the ammonia-evaporation method: Texture, structure, and catalytic performance in hydrogenation of dimethyl oxalate to ethylene glycol, *J. Catal.*, 2008, **257**, 172–180.

42 T. Toupance, M. Kermarec, J.-F. Lambert and C. Louis, Conditions of Formation of Copper Phyllosilicates in Silica-Supported Copper Catalysts Prepared by Selective Adsorption, *J. Phys. Chem. B*, 2002, **106**, 2277–2286.

43 S. Deng, T. Yan, R. Ran, J. Li, G. Zhang and C. Li, Influence of Al Oxides on Cs-SiO2 Catalysts for Vapor Phase Aldol Condensation of Methyl Acetate and Formaldehyde, *Ind. Eng. Chem. Res.*, 2022, **61**, 5766–5777.

44 R. Ran, H. Yan, G. Zhang, Z. Li, G. Wang, G. Wang, W. Su and C. Li, Elucidating the Promotional Effects of the Al Element on the Catalytic Performance of Al–Cs/SiO2 for Methyl Methacrylate Synthesis via One-Step Aldol Condensation, *Ind. Eng. Chem. Res.*, 2024, **63**, 15404–15414.

45 S. Deng, K. Zhao, Q. Li, G. Zhang, J. Li, G. Wang and C. Li, Zirconium-Modified Cs/SiO2 Catalyst for Synthesis of Methyl Acrylate via Aldol Condensation of Methyl Acetate with Formaldehyde, *Ind. Eng. Chem. Res.*, 2024, **63**, 15707–15720.

46 C.-C. Chen, L. Lin, R.-P. Ye, L. Huang, L.-B. Zhu, Y.-Y. Huang, Y.-Y. Qin and Y.-G. Yao, Construction of Cu-Ce composite oxides by simultaneous ammonia evaporation method to enhance catalytic performance of Ce-Cu/SiO2 catalysts for dimethyl oxalate hydrogenation, *Fuel*, 2021, **290**, 120083.

47 R. A. Shawabkeh, N. M. Faqir, K. M. Rawajfeh, I. A. Hussein and A. Hamza, Adsorption of CO2 on Cu/SiO2 nano-catalyst: Experimental and theoretical study, *Appl. Surf. Sci.*, 2022, **586**, 152726.

48 J. Hao, J. Liu, S. Deng, L. Wang, G. Wang and C. Li, Modification of Cs/SiO2 with Zr element through sol–gel method for production of methyl methacrylate via one-step aldol condensation, *Chem. Eng. Sci.*, 2025, **302**, 120899.

49 L. Xu, X. Wang, J. Song, J. Liu and D. Liu, Rational synergetic insight of Cs-Nb/Al2O3 toward promoted catalytic performance in aldol condensation of formaldehyde and methyl propionate, *Chem. Eng. Sci.*, 2025, **302**, 120781.

50 M. Cheng, Y. Wang, W. Wang, G. Wang, X. Zhu and C. Li, Promoting effect of copper oxide on CsX zeolite catalyst for side-chain alkylation of toluene with methanol, *Microporous Mesoporous Mater.*, 2021, **311**, 110732.

51 J. Sackey, L. C. Razanamahandry, S. K. O. Ntwampe, N. Mlungisi, A. Fall, C. Kaonga and Z. Y. Nuru, Biosynthesis of CuO nanoparticles using Mimosa hamata extracts, *Mater. Today: Proc.*, 2021, **36**, 540–548.

52 A. G. Ramu, M. L. A. Kumari, M. S. Elshikh, H. H. Alkhamis, A. F. Alrefaei and D. Choi, A facile and green synthesis of CuO/NiO nanoparticles and their removal activity of toxic nitro compounds in aqueous medium, *Chemosphere*, 2021, **271**, 129475.

53 X. Weng, S. Yang, D. Ding, M. Chen and H. Wan, Applications of in-situ wide spectral range infrared absorption spectroscopy for CO oxidation over Pd/SiO2 and Cu/SiO2 catalysts, *Chin. J. Catal.*, 2022, **43**, 2001–2009.

54 Z. Bian, W. Zhong, Y. Yu, B. Jiang and S. Kawi, Cu/SiO2 derived from copper phyllosilicate for low-temperature water-gas shift reaction: Role of Cu+ sites, *Int. J. Hydrogen Energy*, 2020, **45**, 27078–27088.

55 V. L. Sushkevich, I. I. Ivanova and E. Taarning, Mechanistic Study of Ethanol Dehydrogenation over Silica-Supported Silver, *ChemCatChem*, 2013, **5**, 2367–2373.

56 A. Kumar, A. Ashok, R. R. Bhosale, M. A. H. Saleh, F. A. Almomani, M. Al-Marri, M. M. Khader and F. Tarlochan, In situ DRIFTS Studies on Cu, Ni and CuNi catalysts for Ethanol Decomposition Reaction, *Catal. Lett.*, 2016, **146**, 778–787.

57 J. Shan, J. Liu, M. Li, S. Lustig, S. Lee and M. Flytzani-Stephanopoulos, NiCu single atom alloys catalyze the CH bond activation in the selective non- oxidative ethanol dehydrogenation reaction, *Appl. Catal., B*, 2018, **226**, 534–543.

58 R. Ásmundsson, P. Uvdal and A. D. MacKerell Jr, Binary combination and overtone modes in the C–H stretch region in ethoxy adsorbed on Cu(100): Experimental and calculated vibrational spectra, *J. Chem. Phys.*, 2000, **113**, 1258–1267.

59 F. Zhang, K. Chen, Q. Jiang, S. He, Q. Chen, Z. Liu, J. Kang, Q. Zhang and Y. Wang, Selective Transformation of Methanol to Ethanol in the Presence of Syngas over Composite Catalysts, *ACS Catal.*, 2022, **12**, 8451–8461.

60 J. Fan, J. Yao, X. Feng, C. Wang, Y. Shi, H. Feng, W. Gao, Y. He, X. Guo, S. Yasuda, G. Yang and N. Tsubaki, Unveiling the Catalytic Role of Zeolite P1 in Carbonylation Reaction, *Chem. Bio. Eng.*, 2024, **1**, 141–149.

61 Z. Cheng, S. Huang, Y. Li, K. Cai, Y. Wang, M.-y. Wang, J. Lv and X. Ma, Role of Brønsted Acid Sites within 8-MR of Mordenite in the Deactivation Roadmap for Dimethyl Ether Carbonylation, *ACS Catal.*, 2021, **11**, 5647–5657.

62 Z. Ren, M. N. Younis, H. Zhao, C. Li, X. Yang, E. Wang and G. Wang, Silver modified Cu/SiO2 catalyst for the hydrogenation of methyl acetate to ethanol, *Chin. J. Chem. Eng.*, 2020, **28**, 1612–1622.

63 H. Zhou, W. Zhu, L. Shi, H. Liu, S. Liu, Y. Ni, Y. Liu, Y. He, S. Xu, L. Li and Z. Liu, In situ DRIFT study of dimethyl ether carbonylation to methyl acetate on H-mordenite, *J. Mol. Catal. A: Chem.*, 2016, **417**, 1–9.

64 J. Ding, T. Popa, J. Tang, K. A. M. Gasem, M. Fan and Q. Zhong, Highly selective and stable Cu/SiO2 catalysts prepared with a green method for hydrogenation of diethyl oxalate into ethylene glycol, *Appl. Catal., B*, 2017, **209**, 530–542.

65 S. Wang, L. Song and Z. Qu, Cu/ZnAl2O4 catalysts prepared by ammonia evaporation method: Improving methanol selectivity in CO2 hydrogenation via regulation of metal-support interaction, *Chem. Eng. J.*, 2023, **469**, 144008.

66 J. Luo, T. Xiao, W. Wen, J. Bao, C. Liu and Y. Pan, Effects of Acid Sites and Formaldehyde Decomposition on the Catalyst

Lifetime for Methanol-to-Olefins over Ca-Modified HZSM-5, *ACS Catal.*, 2024, **14**, 14078–14088.

67 J. Duan, S. Fan, X. Li and S. Liu, Enhanced conversion of methane to liquid-phase oxygenates via hollow ferrite nanotube@horseradish peroxidase based photoenzymatic catalysis, *Appl Catal B-Environ.*, 2025, **361**, 124593.

68 X. Wu, R. Chang, M. Tan, L. Tao, Q. Fan, X. Hu, H. L. Tan, M. Åhlén, O. Cheung and W. Liu, An investigation of the Ni/carbonate interfaces on dual function materials in integrated CO2 capture and utilisation cycles, *Appl. Catal., B*, 2023, **338**, 123053.

69 W. Wang, D. Xu, B. Cheng, J. Yu and C. Jiang, Hybrid carbon@TiO2 hollow spheres with enhanced photocatalytic CO2 reduction activity, *J. Mater. Chem. A*, 2017, **5**, 5020–5029.

70 G. Xu and X. Zhu, A core-shell structured Zn/SiO2@ZSM-5 catalyst: Preparation and enhanced catalytic properties in methane co-aromatization with propane, *Appl. Catal., B*, 2021, **293**, 120241.

71 L. Xu, X. Wang, J. Song, J. Liu and D. Liu, Coking and deactivation behavior study of Ce-modified Cs-Nb/Al2O3 in aldol condensation of methyl propionate with formaldehyde, *Mol. Catal.*, 2024, **564**, 114323.

72 Z. Wang, L. Gao, E. Xing, X. Gao, M. Xin, X. Peng, Y. Luo and X. Shu, Preparation of Methyl Acrylate through Catalytic Aldol Condensation over Cs/TS-1 Catalysts, *ACS Sustain. Chem. Eng.*, 2024, **12**, 4876–4886.

73 J. Liu, S. Deng, G. Zhang, J. Li, G. Wang, C. Li and Z. Li, Polyethylene glycol promoted Cs/Zr-SiO2 bifunctional catalyst for aldol condensation of methyl propionate and formaldehyde to methyl methacrylate, *Chem. Eng. J.*, 2024, **499**, 156417.

74 Z. Wu, T. Sun, Z. Li and C. Li, Si-Modified Cs/Al2O3 for Aldol Condensation of Methyl Acetate with Formaldehyde to Methyl Acrylate by Chemical Liquid Deposition, *Ind. Eng. Chem. Res.*, 2022, **61**, 17467–17478.

75 C. Feng, J. Liu, K. Zhao, L. Wang, Z. Li, G. Zhang and C. Li, Influence of pore structure on catalytic performance of Cs-Zr/SiO2 catalyst for methyl methacrylate synthesis from methyl propionate and formaldehyde, *Chem. Eng. Sci.*, 2025, **301**, 120760.

76 R. Ran, W. Zhu, G. Zhang, L. Wang, G. Wang and J. Li, Unraveling the Coking and Deactivation Behavior of Al–Cs/SiO2 Catalyst in the Aldol Condensation of Methyl Propionate with Formaldehyde, *Ind. Eng. Chem. Res.*, 2024, **63**, 1286–1297.

77 B. Zugic, S. Karakalos, K. J. Stowers, M. M. Biener, J. Biener, R. J. Madix and C. M. Friend, Continuous Catalytic Production of Methyl Acrylates from Unsaturated Alcohols by Gold: The Strong Effect of C=C Unsaturation on Reaction Selectivity, *ACS Catal.*, 2016, **6**, 1833–1839.

78 Y. Guan, H. Ma, W. Chen, M. Li, G. Qian, D. Chen, X. Zhou and X. Duan, Methyl Methacrylate Synthesis: Thermodynamic Analysis for Oxidative Esterification of Methacrolein and Aldol Condensation of Methyl Acetate, *Ind. Eng. Chem. Res.*, 2020, **59**, 17408–17416.